*atoms*

MDPI

*Article*

# Computational and Spectroscopic Investigation of Diaminomethane Formation: The Simplest Geminal Diamine of Astrochemical Interest

**Pravi Mishra [1,2], Parmanand Pandey [1,2], Rachana Singh [2], Manisha Yadav [2], Shivani [2], Aftab Ahamad [2], Alka Misra [1,*], Amritanshu Shukla [2] and Poonam Tandon [2]**

[1] Department of Mathematics & Astronomy, University of Lucknow, Lucknow 226007, India; pravimishra231@gmail.com (P.M.); parmanand.physics@gmail.com (P.P.)
[2] Department of Physics, University of Lucknow, Lucknow 226007, India; singh.rchncat@gmail.com (R.S.); yadavmanisha605@gmail.com (M.Y.); physics.shiv@gmail.com (S.); aftabhmd710@gmail.com (A.A.); amritanshushukla@gmail.com (A.S.); tandon_poonam@lkouniv.ac.in (P.T.)
* Correspondence: alkamisra99@gmail.com; Tel.: +91-9415580700

**Abstract**

A high-level ab initio characterization and formation of diaminomethane (DAM), the simplest geminal diamine, is presented to support its spectroscopic detection and astrochemical relevance in the interstellar medium. The $C_{2v}$ DAM conformer is identified as the global minimum, while $C_1$ DAM and $C_2$ DAM represent higher-energy local minima. The proposed reaction pathways are exothermic and proceed without activation barriers. Simulated infrared spectrum reproduces accurate key spectral signatures with several vibrational modes exhibiting strong IR intensities (>80 km mol$^{-1}$), particularly in the 800–3000 cm$^{-1}$ range and band shapes. Dipole moments and accurate rovibrational spectroscopic parameters, including rotational constants, anharmonic vibrational frequencies, quartic and sextic distortion constants, and nuclear quadrupole coupling constants are reported to assist with high-resolution spectroscopic identification. This study provides significant theoretical benchmarks for its formation and offers guidance for future laboratory spectroscopy and molecular searches in interstellar environments.

**Keywords:** astrobiology; astrochemistry; ISM: molecules; ISM: abundances; complex organic molecules; quantum chemistry; amines; diaminomethane

check for updates

Academic Editor: Pascal Quinet

Received: 5 August 2025
Revised: 3 October 2025
Accepted: 4 November 2025
Published: 12 November 2025

**Citation:** Mishra, P.; Pandey, P.; Singh, R.; Yadav, M.; Shivani; Ahamad, A.; Misra, A.; Shukla, A.; Tandon, P. Computational and Spectroscopic Investigation of Diaminomethane Formation: The Simplest Geminal Diamine of Astrochemical Interest. *Atoms* **2025**, *13*, 91. https://doi.org/10.3390/atoms13110091

**Copyright:** © 2025 by the authors. Licensee MDPI, Basel, Switzerland. This article is an open access article distributed under the terms and conditions of the Creative Commons Attribution (CC BY) license (https://creativecommons.org/licenses/by/4.0/).

## 1. Introduction

A rising number of $NH_3$, $NH_2$, and NH-bearing species have been identified recently in the galactic core, increasing the likelihood of discovering different prebiotic complex organics in interstellar space [1]. Nitrogen-bearing complex organic molecules are particularly significant in terms of understanding the prebiotic chemistry of the interstellar medium (ISM) since they can be considered as an intermediary step in the production of biologically significant species such as nucleobases and amino acids [2].

In this context, nitrogen-rich species with geminal substitution patterns are especially intriguing, as they may represent key structural motifs in the progression toward biochemical complexity. Several such interstellar molecules featuring geminal substitution patterns have been identified in molecular clouds. Among these, acetone $(CH_3)_2CO$) has been observed towards hot cores such as Sgr B2(N) [3]. By contrast, aminoacetonitrile ($NH_2CH_2CN$) [4] and aminomethanol ($NH_2CH_2OH$), described as disubstituted methanes,

are also key precursors in Strecker-type glycine formation, and have been detected in the same source. However, structurally simpler geminal diamines remain notably absent from the current interstellar inventory. Molecules such as diaminomethane ($(NH_2)_2CH_2$) represent such minimal geminal amine architectures. Among known N–C–N type interstellar molecules, viz. cyanamide ($H_2N–C{\equiv}N$) [5], carbodiimide (HN=C=NH) [6], and urea ($(NH_2)_2CO$ [7], diaminomethane is the only fully saturated and symmetric diamine with such a backbone, where both $–NH_2$ groups are bonded to a central $–CH_2–$ carbon.

Diaminomethane (hereafter referred to as DAM) is of particular astrochemical interest due to its bifunctional nature and compact geometry, allowing it to engage in both hydrogen bonding and radical recombination chemistry. Theoretical studies suggest that the structural simplicity of such species, coupled with their large dipole moments and active rotational spectra across the infrared to microwave range, makes them highly significant for detection via millimeter and submillimeter–wave radioastronomy in the interstellar medium [8–11]. Despite this astrochemical relevance, the conformational flexibility of DAM and its implications for detectability have not been fully addressed. An experimental study on DAM was performed by Marks et al. [12], in which they successfully synthesized DAM ($CH_2(NH_2)_2$) and characterized its spectroscopic properties. Their findings suggest that DAM could serve as a potential precursor to nucleobases in the interstellar medium [12]. Following this, a study addressing the detectability of DAM in the interstellar medium [13] has been reported, raising a question of further probability of finding more complex amines containing molecules in the space. Watrous et al. [13] provided the rotational constants for the $C_1$ and $C_2$ conformers, along with IR frequencies for the $C_{2v}$ conformer for comparison with the experimental results obtained by Marks et al. [12]. While the conformational landscape of DAM has previously been investigated, including the identification of three minima on its potential energy surface, namely, a global minimum with $C_{2v}$ symmetry (most stable), a higher-lying $C_2$ conformer above the minimum, and a higher-energy (less stable) $C_1$ conformer [12]. Previous high-level quantum chemical investigations, such as those by Watrous et al. [13], have restricted their analysis to the most stable $C_{2v}$ form, largely in the context of benchmarking electronic structure methods. However, the astrochemical relevance and spectroscopic properties of the higher-energy conformers remain unexplored.

In this work, we address this gap by investigating the formation pathways of all three conformers under interstellar conditions. Specifically, we characterize the minimum energy geometries and harmonic vibrational spectra, compute rotational constants and dipole moments, and investigate formation pathways relevant to interstellar environments to support future observational identification. In particular, the formation of all three conformers of DAM is explored through radical–radical reaction mechanisms in the gas phase involving highly abundant and previously detected interstellar radicals. This choice is motivated by the well-established prevalence of such radicals (e.g., $NH_3$, $NH_2$, NH, $CH_4$, $CH_2$) in various astrophysical environments, which enhances the thermodynamic feasibility and kinetic accessibility of the proposed pathways. This comprehensive analysis establishes a molecular level framework for understanding the stability, detectability, and formation dynamics of DAM in astrochemical environments.

## 2. Methodology

### *2.1. Geometry Optimization and Vibrational Analysis*

The molecular geometries of all relevant species including reactants, products were optimized using the B2PLYPD [14] functional in conjunction with the aug–cc–pVTZ basis set [15]. These methods were selected based on their ability to account for long-range dispersion interactions and their proven accuracy in astrochemical modeling. Vibrational

frequency analyses at the same level of theory confirmed the nature of each optimized structure. Stationary points with no imaginary frequencies were confirmed as minima.

To improve the accuracy of the computed electronic energies, single-point energy calculations were performed at the CCSD [16–18] method in conjunction with aug–cc–pVTZ level using the B2PLYPD-optimized geometries. Additional calculations at the MP2/aug–cc–pVTZ [19–23] level were carried out to enable method comparison.

DFT-based quantum chemical computations provide a computationally efficient means of estimating energies and other chemical parameters with moderate accuracy. When modeling the interstellar formation of complex molecules, these reference approaches are frequently used [24–36]. Computational methods used in this study were mostly guided by benchmarking data from the literature, particularly those related to reactions involving radical species and nitrogen-containing functional groups [37–39]. The functional employed in our calculations provides a balanced description of energies and molecular properties, while higher-level coupled cluster methods were used where greater accuracy was required.

### *2.2. Reaction Energetics and Rate Constants*

To assess the kinetic feasibility of the reaction mechanisms, potential energy surface (PES) scans were performed along relevant reaction coordinates to locate barrierless and exothermic pathways. The relative energies (ΔE) are computed as adiabatic differences between the energies plus corresponding ZPVEs of the optimized products and reactants.

Standard thermodynamic parameters including internal energy (ΔU), enthalpy (ΔH), and Gibbs free energy (ΔG) were computed at 298.150 K temperature and 1 atm using vibrational frequency data. Thermal corrections were included, and the net changes in these parameters for each reaction were calculated as follows:

$$\textit{Change in Internal energy } (\Delta U) = \sum \Delta U_{products} - \sum \Delta U_{reactants}$$

$$\textit{Change in Enthalpy } (\Delta H) = \sum \Delta H_{products} - \sum \Delta H_{reactants}$$

$$\textit{Change in Gibbs Free Energy } (\Delta G) = \sum \Delta G_{products} - \sum \Delta G_{reactants}$$

For $\Delta U, \Delta G, \Delta H < 0$, the reactions are exergonic and spontaneous.

Also, rate constants for the elementary steps were estimated using the Langevin capture theory [40], suitable for radical–radical interactions, as follows:

$$k = 7.14 \times 10^{-10} \alpha^{1/2} (10/\mu)^{1/2} \text{ cm}^3 \text{ s}^{-1}$$

where α is the polarizability (in $Å^3$) and μ is the reduced mass (in $^{12}C$ amu). This approach, based on the Bates formalism, provides temperature-independent estimates suitable for interstellar conditions.

### *2.3. Vibro–Rotational and Nuclear Quadrupole Properties*

Dipole moments and vibro–rotational constants including quartic and sextic distortion constants were computed at the ωB97XD/aug–cc–pVQZ level. A complete vibrational analysis including harmonic and anharmonic corrections was performed. Additionally, nuclear quadrupole coupling constants were calculated using the NMR module in Gaussian 16 at the same level of theory. Where available, these data were compared with experimental and theoretical values to ensure the reliability of predicted spectroscopic observables.

### *2.4. Spectroscopic Analysis: Infrared Spectroscopic Analysis*

The infrared vibrational spectra of the $C_1$, $C_2$, and $C_{2v}$ isomers of DAM were computed at the B2PLYPD/aug–cc–pVTZ level of theory. To simulate the IR spectra, a universal scaling factor of 0.9862 was applied to the computed harmonic frequencies to account for anharmonic effects and basis set deficiencies. The resulting spectra were convolved using a Gaussian line shape function with a full width at half maximum (FWHM) of 25 $cm^{-1}$, allowing for direct comparison with experimental or observational data.

The computational framework used in this work enabled a detailed exploration of the thermodynamic and kinetic aspects of the proposed reaction mechanisms. Four reaction pathways were identified as exothermic and barrierless, suggesting their significance in the formation of DAM under astrophysical conditions. Computational investigations were carried out using the Gaussian 16 program package [41].

## 3. Computational Result and Discussions

### *3.1. Reaction Mechanism and Potential Energy Profiles (PES)*

The formation of DAM ($CH_2(NH_2)_2$) in the interstellar medium (ISM) can occur through different reaction pathways involving radicals, viz. NH, $NH_2$, $CH_4$, $CH_3$, $CH_2$, and $CH_3NH_2$ in the gas phase. The key reactants have all been detected in the ISM. These reactions are driven by the highly reactive nature of radicals and the low-temperature conditions typical of interstellar clouds, where activation barriers are minimized due to radical–radical recombination mechanisms [42].

Table 1 presents the total energies (in a.u. and kJ/mol) of the reactants and products at different computational levels (B2PLYPD and MP2) and same basis set. Additionally, the calculated rate constants at the temperature of 298.15 K for each reaction pathway are listed in Table 2, providing insights into the thermodynamic feasibility and kinetics of these reactions. The four exothermic and barrierless reaction routes are predicted for the formation of DAM. Figure 1 schematically represents the reaction mechanisms, illustrating the reactants and final products along each reaction route. The reaction pathways are color-coded: red for Reaction 1, green for Reaction 2, black for Reaction 3, and blue for Reaction 4.

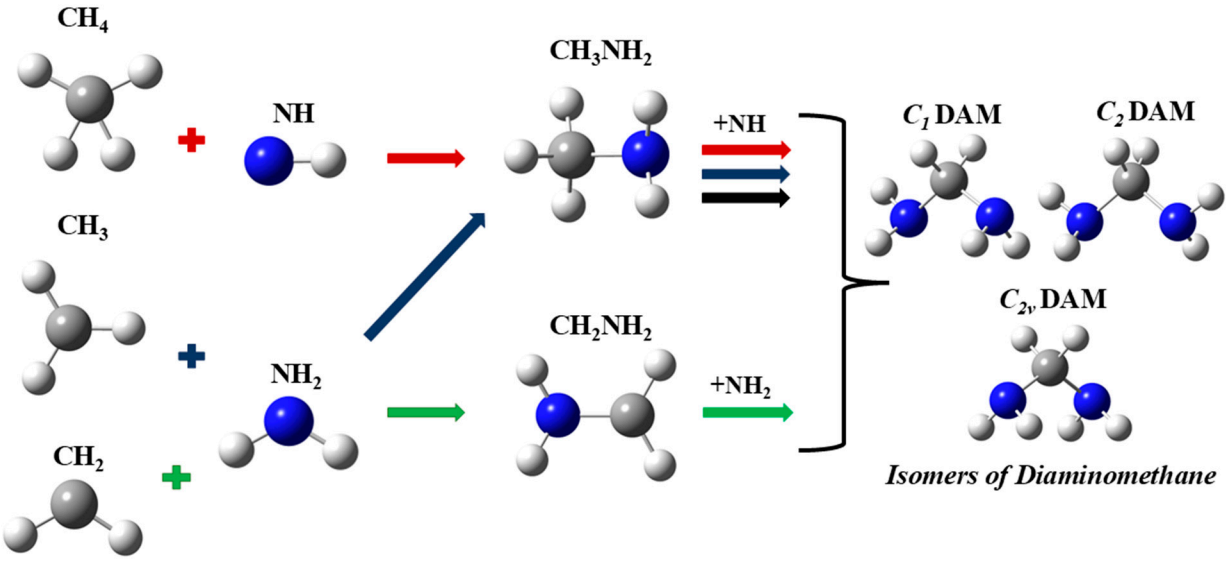



**Figure 1.** Schematic representation of reactants and products involved in the reaction pathways (Reaction 1–Red, Reaction 2–Green, Reaction 3–Black, Reaction 4–Blue). The same-colored arrows represent particular reaction routes. Color representations for atoms are gray–carbon, white–hydrogen, and blue–nitrogen.

**Table 1.** Total energies (a.u.) and relative energies in kJ/mol for the DAM at B2PLYPD/aug–cc–pVTZ and MP2/aug–cc–pVTZ level of DFT is listed.

| | DAM ($CH_2(NH_2)_2$) | | | |
|---|---|---|---|---|
| | B2PLYPD | | MP2 | |
| **Reactants/Products** | **Total Energy** | **Relative Energy** | **Total Energy** | **Relative Energy** |
| $CH_2$ | −39.092 | – | −39.017 | – |
| $CH_3$ | −39.783 | – | −39.708 | – |
| $CH_4$ | −40.443 | – | −40.369 | – |
| NH | −55.114 | – | −55.030 | – |
| $NH_2$ | −55.839 | – | −55.757 | – |
| $CH_3NH_2$ | −95.749 | – | −95.602 | – |
| | | **Reaction-1** | | |
| $CH_4$ + NH (R) | −95.557 | – | −95.399 | – |
| $CH_3NH_2$ (P) | −95.749 | −503.190 | −95.602 | −533.462 |
| $CH_3NH_2$ + NH (R) | −150.863 | – | −150.633 | – |
| $C_1$ DAM (P) | −151.069 | −541.436 | −150.851 | −573.572 |
| | | **Reaction-2** | | |
| $CH_2$ ($^1A_1$) + $NH_2$ (R) | −94.931 | – | −94.775 | – |
| $CH_2NH_2$ (P) | −95.108 | −465.123 | −94.959 | −484.363 |
| $CH_2NH_2$ + $NH_2$ (R) | −150.948 | – | −150.716 | – |
| $C_{2v}$ DAM (P) | −151.070 | −321.495 | −150.852 | −356.144 |
| | | **Reaction-3** | | |
| $CH_3NH_2$ + NH (R) | −150.863 | – | −150.633 | – |
| $C_1$ DAM (P) | −151.069 | −541.436 | −150.851 | −573.564 |
| | | **Reaction-4** | | |
| $CH_3$ + $NH_2$ (R) | −95.622 | – | −95.465 | – |
| $CH_3NH_2$ (P) | −95.749 | −333.460 | −95.602 | −360.114 |
| $CH_3NH_2$ + NH (R) | −150.863 | – | −150.633 | – |
| $C_2$ DAM (P) | −151.069 | −541.441 | −150.851 | −572.107 |

**Table 2.** Calculated rate constants for DAM at B2PLYPD/aug−cc−pVTZ level of DFT is listed.

| Reaction | Molecules | Rate Constants ($cm^3\ s^{-1}$) |
|---|---|---|
| **Reaction−1** | $CH_4$ + NH → $CH_3NH_2$ | $4.137 \times 10^{-10}$ |
| | $CH_3NH_2$ + NH → $C_1$ DAM | $4.262 \times 10^{-10}$ |
| **Reaction−2** | $CH_2$ + $NH_2$ → $CH_2NH_2$ | $4.321 \times 10^{-10}$ |
| | $CH_2NH_2$ + $NH_2$ → $C_{2v}$ DAM | $4.194 \times 10^{-10}$ |
| **Reaction−3** | $CH_3NH_2$ + NH → $C_1$ DAM | $4.262 \times 10^{-10}$ |
| **Reaction−4** | $CH_3$ + $NH_2$ → $CH_3NH_2$ | $4.137 \times 10^{-10}$ |
| | $CH_3NH_2$ + NH → $C_2$ DAM | $4.262 \times 10^{-10}$ |

Figures 2–5 represent potential energy surface (PES) profiles for the formation of DAM via multiple radical-mediated reaction pathways under interstellar conditions. Each figure

depicts graphs of a two–step process with energy variations along the reaction coordinate. The blue lines represent the first step (radical–radical recombination or hydrogen abstraction forming intermediates viz. $CH_3NH_2$ or $CH_2NH_2$), while the red lines represent the second step leading to different isomers of DAM ($C_1$, $C_2$, or $C_{2v}$).

### *3.2. Reaction Routes*

**Reaction 1: From Methane ($CH_4$) and Imidogen (NH)**

$$\mathbf{CH_4 + NH \rightarrow CH_3NH_2}$$

$$\mathbf{CH_3NH_2 + NH \rightarrow CH_2(NH_2)_2}$$

In the first pathway, $CH_4$ is a closed-shell, tetrahedral molecule and NH is a radical, highly reactive due to its singly occupied molecular orbital acting as initial reactants. Methane ($CH_4$) reacts with imidogen (NH) to form methylamine ($CH_3NH_2$). The reaction proceeds with energy $-503.190$ kJ/mol relative to reactants, indicating strong exoergicity and a rate constant of $4.137 \times 10^{-10}$ $cm^3s^{-1}$. This occurs via hydrogen abstraction facilitated by the NH radical, which acts as a hydrogen acceptor, cleaving a C–H bond in $CH_4$ to form $CH_3$ radical and $NH_2$. Barrierless recombination occurs as the unpaired electrons pair to form the C–N bond. The PES (Figure 2) shows a steep energy well corresponding to the bond dissociation and abstraction process. The resulting $CH_3NH_2$ then undergoes a second reaction with another NH radical, where a hydrogen is abstracted from the methyl group, leading to the formation of $C_1$ DAM. This pathway is highly exothermic, with relative energy of $-541.436$ kJ/mol and a rate constant of $4.262 \times 10^{-10}$ $cm^3s^{-1}$, and occurs without significant activation barriers, making it feasible under the low-temperature conditions of dense molecular clouds.

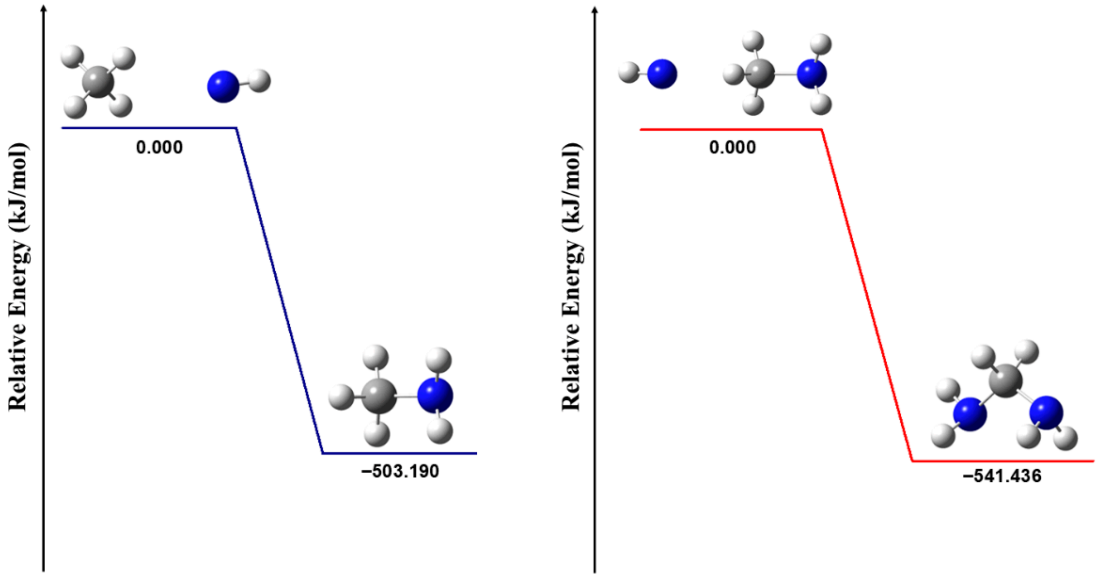



**Figure 2.** Schematic potential energy surface (PES) diagrams for the stepwise formation of $C_1$ DAM from methane ($CH_4$) and imidogen (NH). Relative energies (in kJ/mol) are computed at B2PLYPD/aug–cc–pVTZ.

**Reaction 2: From Methylene ($CH_2$) and Amidogen ($NH_2$)**

$$\mathbf{CH_2 + NH_2 \rightarrow CH_2NH_2}$$

$$\mathbf{CH_2NH_2 + NH_2 \rightarrow CH_2(NH_2)_2}$$

In this reaction route, $CH_2$ and $NH_2$ are both open–shell radicals. Methylene ($CH_2$), a known reactive intermediate in the ISM, reacts directly with $NH_2$ via radical–radical recombination to form the $CH_2NH_2$ radical, forming a σ bond between carbon and nitrogen. Reactions of both $CH_2$ in its triplet ($^3B_1$) and singlet ($^1A_1$) electronic states with the amino radical ($NH_2$) have been investigated, considering the possibility of spin-dependent reactivity. Although $CH_2$ ($^3B_1$) is the electronic ground state of methylene in isolation, our results indicate that the $CH_2NH_2$ adduct formed via the singlet ($^1A_1$) pathway is more stable by ~191.7 kJ $mol^{-1}$ than that obtained through the triplet ($^3B_1$) pathway. Thus, while both electronic states of $CH_2$ can, in principle, react with $NH_2$, the singlet channel is thermodynamically preferred.

It should be noted that in order for the triplet $CH_2$ ($^3B_1$) to participate in the reaction, an intersystem crossing ($^3B_1 \rightarrow {}^1A_1$) must first occur to conserve spin. This excitation introduces an energetic cost, effectively acting as a kinetic barrier to the triplet channel. In contrast, the reaction involving singlet $CH_2$ ($^1A_1$) with $NH_2$ proceeds without requiring spin inversion, leading to a barrierless and thermodynamically more favorable pathway. Consequently, while both reaction routes yield $CH_2NH_2$, the singlet pathway dominates under astrochemical conditions, whereas the triplet pathway may contribute only under circumstances where intersystem crossing is facilitated, such as on dust grains or via collisional processes.

PES (Figure 3) shows a direct plunge from reactants to a deep minimum corresponding to $CH_2NH_2$. This step releases −465.123 kJ/mol and has a rate constant of 4.321 $\times 10^{-10}$ $cm^3s^{-1}$. The radical then undergoes a secondary recombination with another $NH_2$ radical, yielding $C_{2v}$ DAM with a relative energy of −321.495 kJ/mol and a rate constant of 4.194 $\times 10^{-10}$ $cm^3s^{-1}$. This step also lacks a transition state, with smooth energetic descent. $C_{2v}$ DAM is the most stable isomer thermodynamically. This pathway demonstrates high reactivity of the $CH_2$ radical and the absence of activation barriers in radical–radical interactions, leading to the formation of $C_{2v}$ DAM.

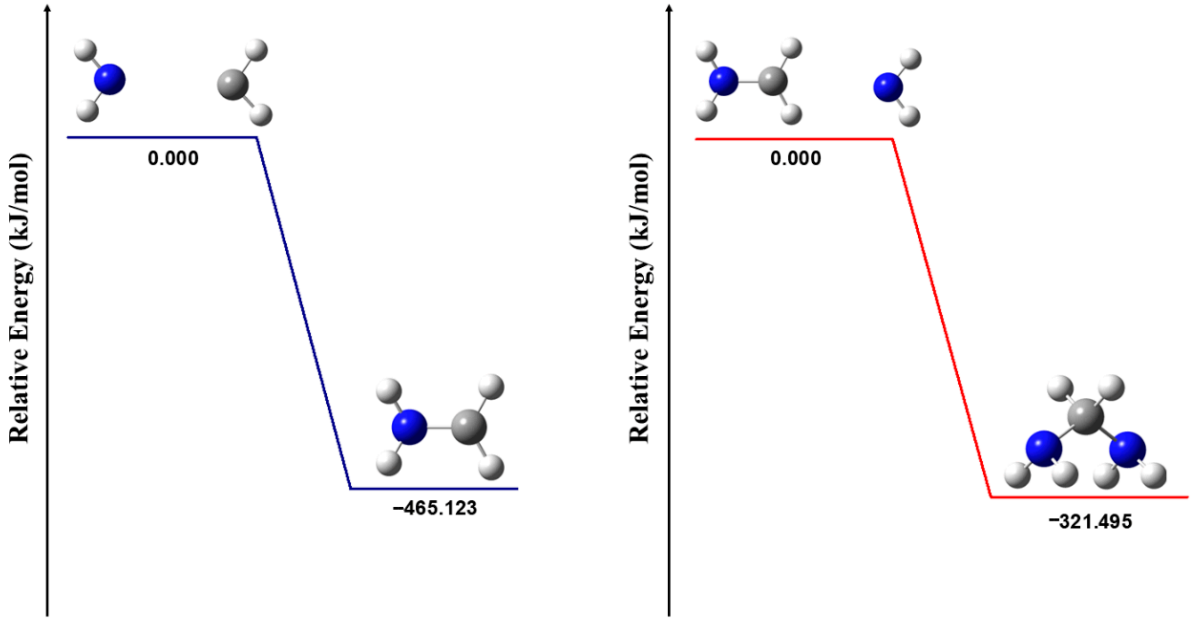



**Figure 3.** Schematic potential energy surface (PES) diagrams for the stepwise formation of $C_{2v}$ DAM from methylene ($CH_2$) and amidogen ($NH_2$). Relative energies (in kJ/mol) are computed at B2PLYPD/aug–cc–pVTZ.

**Reaction 3: Direct Amination of Methylamine ($CH_3NH_2$)**

$$\mathbf{CH_3NH_2 + NH \rightarrow CH_2(NH_2)_2}$$

This is the most straightforward reaction, where methylamine ($CH_3NH_2$) directly reacts with an NH radical. Here, NH abstracts a hydrogen from the methyl group, forming the $CH_2NH_2$ radical, which then recombines with another $NH_2$ radical to produce $C_1$ DAM. The reaction is exothermic, with energy of $-541.436$ kJ/mol relative to the reactants and a rate constant of $4.262 \times 10^{-10}$ $cm^3s^{-1}$. The entire PES (Figure 4) from $CH_3NH_2$ is one transition followed by a barrierless recombination. This pathway bypasses the need for complex intermediates, making it a potentially dominant formation mechanism in environments with high NH and $CH_3NH_2$ abundances.

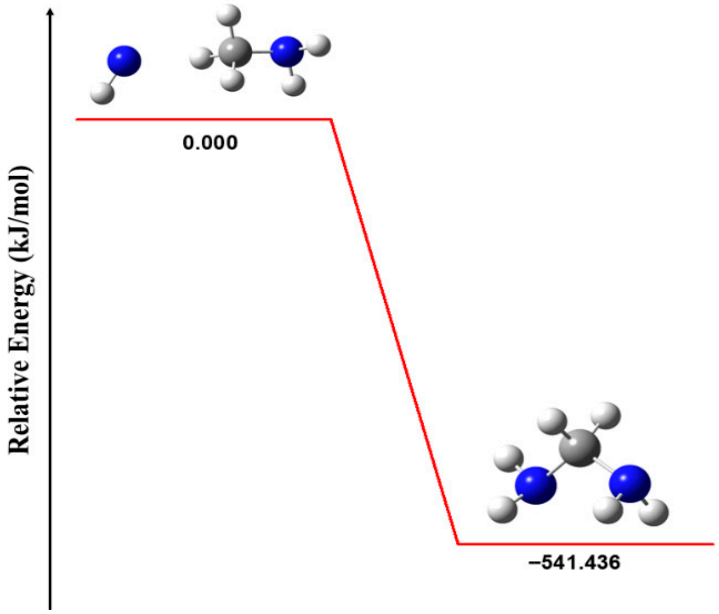



**Figure 4.** Schematic potential energy surface (PES) diagrams for the formation of $C_1$ DAM from direct amination of methylamine ($CH_3NH_2$). Relative energies (in kJ/mol) are computed at B2PLYPD/aug–cc–pVTZ.

**Reaction 4: From Methyl ($CH_3$) and Amidogen ($NH_2$)**

$$\mathbf{CH_3 + NH_2 \rightarrow CH_3NH_2}$$

$$\mathbf{CH_3 + NH_2 \rightarrow CH_3NH_2}$$

The fourth pathway involves the reaction of the methyl radical ($CH_3$) with $NH_2$, forming $CH_3NH_2$ through a direct radical combination. PES (Figure 5) reflects a steep descent to $CH_3NH_2$. This intermediate then reacts with NH through a mechanism analogous to Pathway 1, involving hydrogen abstraction and radical stabilization to ultimately form DAM ($C_2$ DAM). The $CH_3$ + $NH_2$ step has relative energy of $-333.460$ kJ/mol and a rate constant of $4.137 \times 10^{-10}$ $cm^3s^{-1}$, while the conversion to $C_2$ DAM releases $-541.441$ kJ/mol, occurring at $4.262 \times 10^{-10}$ $cm^3s^{-1}$. This highlights the role of NH as both a hydrogen abstractor and a stabilizing agent in the ISM.

All routes are energetically favorable. Across all four reactions, the PES profiles are characterized by strong exergonicity, making these pathways chemically viable under ISM conditions where thermal barriers cannot be overcome and relevant to the astrochemical origins of prebiotic molecules. The PES for each pathway is minimally activated and

shaped by the radical character of the species involved. Rate constants are consistently high, supporting barrierless kinetics, and matching radical-driven ISM processes.

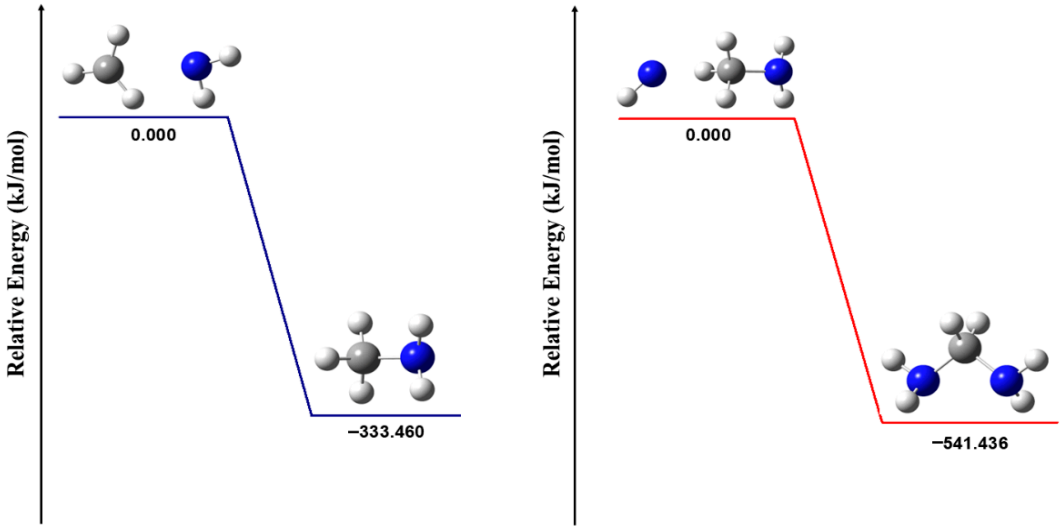



**Figure 5.** Schematic potential energy surface (PES) diagrams for the stepwise formation of $C_2$ DAM from methyl ($CH_3$) and amidogen ($NH_2$). Relative energies (in kJ/mol) are computed at B2PLYPD/aug–cc–pVTZ.

The computed total energies, reaction energies, and rate constants for the reactants, intermediates, and products show slight variations due to the difference in electron correlation treatment between these two levels of theory. The total energies of all species computed using the B2PLYPD functional are consistently lower (more negative) compared to those obtained from MP2. This suggests that B2PLYPD predicts a more stable electronic structure for these molecules than MP2. The total energy differences between the two functionals are ~572 kJ/mol, with B2PLYPD consistently computing lower energy (more stabilized) values relative to MP2. Given these observations, B2PLYPD appears to be the more reliable functional for modeling DAM formation under ISM conditions.

### *3.3. Conformers Energetics and Electronic Analysis*

The computed dipole moments (μ), mean polarizabilities (α), and thermochemical functions; internal energy (ΔU), enthalpy (ΔH), and Gibbs free energy (ΔG) for the three conformers of DAM are summarized in Table 3. Calculations were performed using B2PLYPD/aug−cc−pVTZ and MP2/aug−cc−pVTZ levels of theory. The parameters reveal a strong energetic preference for the $C_1$ DAM and $C_2$ DAM. The results indicate that $C_{2v}$ DAM is the most stable conformer, while $C_1$ DAM and $C_2$ DAM are nearly isoenergetic, with energy differences $\leq$ 3.6 kJ mol$^{-1}$. Such small energy separations suggest that under interstellar conditions, all three conformers may be populated, but $C_{2v}$ DAM is expected to dominate, which is consistent with the barriers to interconversion and the hindered-rotor dynamics. At both levels of theory, the $C_{2v}$ DAM conformer exhibits the highest dipole moment, with values of 1.760 D (B2PLYPD) and 1.835 D (MP2), suggesting a greater permanent charge separation. The lower symmetry $C_1$ DAM and $C_2$ DAM conformers exhibit slightly reduced dipole moments, with nearly identical values (~1.65 D at B2PLYPD and ~1.73–1.57 D at MP2), reflecting slight structural reorientations of the $NH_2$ groups. The polarizability values are nearly invariant across all conformers and computational levels, ranging between 5.241 and 5.336 Å$^3$, indicating minimal conformational influence on the overall electron cloud deformability.

**Table 3.** Dipole moment (μ) in debye (D), polarizability (α) in Å$^3$, relative energy (ΔE), internal energy (ΔU), enthalpy (ΔH), and Gibbs free energy (ΔG) relative to $C_{2v}$ DAM in kJ/mol at MP2/aug–cc–pVTZ is listed.

| Conformers | μ (D) | α (Å$^3$) | ΔE | ΔU | ΔH | ΔG |
|---|---|---|---|---|---|---|
| $C_{2v}$ DAM | 1.835 | 5.243 | 0.000 | 0.000 | 0.000 | 0.000 |
| $C_1$ DAM | 1.733 | 5.241 | 2.087 | 2.255 | 2.253 | 1.901 |
| $C_2$ DAM | 1.569 | 5.247 | 3.547 | 3.571 | 3.568 | 3.571 |

Table 4 details the dipole moment components ($\mu_a$, $\mu_b$, $\mu_c$) along the principal rotational axes for all three conformers, computed at the MP2/aug−cc−pVTZ level, and compared with the literature values [12]. In the $C_{2v}$ DAM, the dipole moment is strictly oriented along the b-axis ($\mu_b$ = −1.835 D), in agreement with its symmetric geometry and previous reports (μ = 1.72 D). The negligible components along $\mu_a$ and $\mu_c$ reflect its planarity and the presence of a mirror plane perpendicular to the dipole vector. The $C_1$ DAM conformer, being asymmetric and non-planar, exhibits significant dipole components along all three axes ($\mu_a$ = 1.279 D, $\mu_b$ = −0.180 D, $\mu_c$ = −1.157 D), resulting in a spatially distributed dipole (μ = 1.735 D). Such anisotropy in dipole orientation implies enhanced polar interactions and may affect its spectroscopic and condensed phase behavior. For the $C_2$ DAM, the dipole vector is predominantly aligned along the b-axis ($\mu_b$ = 1.569 D) with minor components along other axes, resembling the $C_{2v}$ form in orientation but with a reduced magnitude, indicating some preservation of directional charge separation despite its lowered symmetry.

**Table 4.** Total dipole moment and their components ($\mu_a$, $\mu_b$, and $\mu_c$) in debye (D) for $C_{2v}$, $C_1$, and $C_2$ DAM are computed at MP2/aug–cc–pVTZ level of theory and are listed.

| Constant and Unit | $C_{2v}$ DAM | | $C_1$ DAM | | $C_2$ DAM | |
|---|---|---|---|---|---|---|
| | Previous Work [12] | This Work | Previous Work [12] | This Work | Previous Work [12] | This Work |
| Dipole (D) | 1.72 | 1.8353 | 1.22 | 1.7345 | 1.53 | 1.5687 |
| $\mu_a$ (D) | – | −0.0006 | – | 1.2794 | – | 0.0011 |
| $\mu_b$ (D) | – | −1.8353 | – | −0.1798 | – | 1.5687 |
| $\mu_c$ (D) | – | −0.0018 | – | −1.1573 | – | 0.0007 |

### *3.4. Conformational Analysis*

A comprehensive potential energy surface (PES) scan of $C_1$ DAM and $C_2$ DAM was performed with B2PLYPD in combination with the aug-cc-pVTZ basis set by systematically varying the dihedral coordinates defining the relative orientations of the amino groups with respect to the central methylene unit. This scan generated a discretized hypersurface that describes the conformational landscape of the molecule. Stationary points (minima and transition states) were located along the scan and were characterized by harmonic frequency analysis. Minima have no imaginary frequencies and transition states have a single imaginary frequency (frequency analyses were performed at the same level as the optimizations). The optimized geometries of the minima and transition states are shown in Figure 6, illustrating the torsional motion of the amino groups leading to conformational exchange.

The PES of $C_1$ DAM reveals one distinct minimum $C_2$ DAM separated by one transition state (TS1). The $C_2$ DAM scan produced multiple stationary points that we identify here using the labels provided; $C_2$ DAM as reference minimum; $C_1$ DAM as local minimum; $C_{2v}$ DAM as global minimum; and TS1 and TS2 as transition states. $C_2$ DAM (reference minimum) is a relatively stable conformation representing a gauche–gauche

arrangement of the amino groups. $C_1$ DAM (local minimum) is nearly isoenergetic with $C_2$ DAM ($-1.3$ kJ mol$^{-1}$ relative), likely corresponding to a different orientation of the $NH_2$ groups, such as a trans-gauche form. $C_{2v}$ DAM (global minimum) is the most stable conformation ($-3.3$ kJ mol$^{-1}$ relative), exhibiting a near-planar arrangement stabilized by weak intramolecular N–H···N interactions. The transition states TS1 and TS2 in $C_1$ DAM and $C_2$ DAM respectively represent torsional barriers separating minima. In the $C_1$ DAM scan, TS1 (15.4 kJ mol$^{-1}$) connects $C_1$ DAM ↔ $C_2$ DAM, whereas in the $C_2$ DAM scan, TS1 (14.0 kJ mol$^{-1}$) connects $C_2$ DAM ↔ $C_1$ DAM, corresponding to the internal rotation of one amino group. TS2 (9.6 kJ mol$^{-1}$) connects $C_2$ DAM ↔ $C_{2v}$ DAM, allowing direct relaxation into the global minimum geometry. The global minimum $C_{2v}$ DAM is calculated to be ≈3.3 kJ mol$^{-1}$ more stable than the $C_2$ DAM reference and ≈2.0 kJ mol$^{-1}$ more stable than $C_1$ DAM.

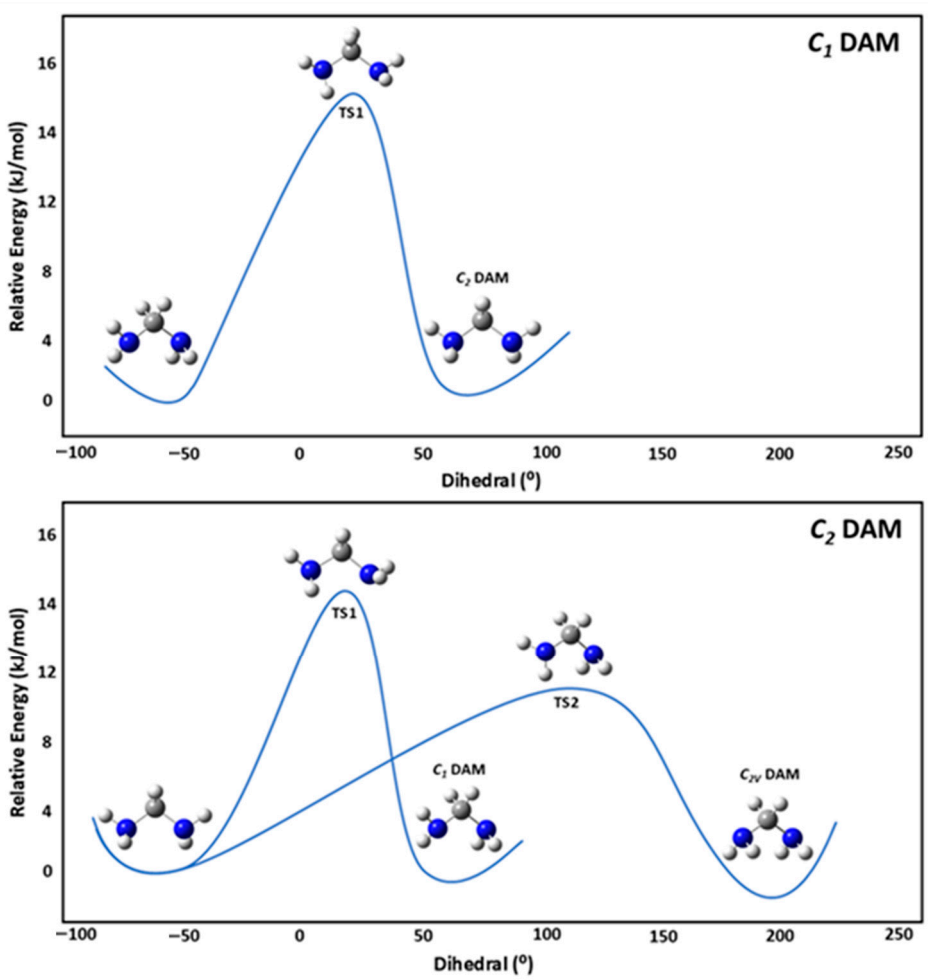



**Figure 6.** Potential energy surface of $C_1$ DAM and $C_2$ DAM scan at the B2PLYPD/aug-cc-pVTZ level, depicting the optimized geometries of the conformers and transition states obtained along the scan. Relative energies are shown in kJ mol$^{-1}$.

These energy differences are small and the stabilization of $C_{2v}$ DAM relative to other minima is consistent with intramolecular N–H···N interactions that reduce repulsion between lone pairs on the amino groups and permit a lower-energy conformation. The scan shows DAM exists in several nearly degenerate conformations, separated by small barriers of ~10–15 kJ mol$^{-1}$. In the interstellar medium, both thermal energy and tunneling are sufficient to ensure conformer exchange, shaping DAM's observable spectra and its reactivity in astrochemical environments.

### 3.5. Rotational Spectroscopic Constants

The equilibrium and vibrationally corrected rotational constants (*A*, *B*, and *C*), along with quartic and sextic centrifugal distortion constants for $C_{2v}$, $C_1$, and $C_2$ DAM, were computed at ωB97XD/aug–cc–pVTZ level of theory. Also, nuclear quadrupole coupling constants including vibrational corrections are computed using NMR at the same level of theory. These data are summarized in Table 5. For comparison, the literature values for the equilibrium constants of the symmetric $C_{2v}$ DAM conformer are also included. The calculated values are in good agreement with Marks et al.'s previous work [12].

**Table 5.** Rotational constants (*A*, *B*, and *C*) and quartic, sextic, and nuclear quadrupole coupling constants including vibrational corrections for $C_{2v}$, $C_1$, and $C_2$ DAM are computed at ωB97XD/aug–cc–pVTZ level of theory and are listed.

| Constant and Unit | $C_{2v}$ DAM | | $C_1$ DAM | $C_2$ DAM |
|---|---|---|---|---|
| | Previous Work [13] | This Work | This Work | This Work |
| $A_e$ (MHz) | 35,538.7 | 35,494.405 | 36,203.369 | 36,489.639 |
| $B_e$ (MHz) | 9156.0 | 9081.374 | 9278.307 | 9654.229 |
| $C_e$ (MHz) | 8287.9 | 8230.010 | 8269.962 | 8384.761 |
| $A_0$ (MHz) | 35,248.8 | 35,293.297 | 35,868.671 | 36,133.097 |
| $B_0$ (MHz) | 9056.7 | 8978.241 | 9184.659 | 9562.709 |
| $C_0$ (MHz) | 8191.6 | 8135.291 | 8183.081 | 8293.224 |
| $\Delta_J$ (kHz) | 8.039 | 7.645 | 8.168 | 8.184 |
| $\Delta_K$ (kHz) | 243.619 | 240.102 | 262.191 | 258.454 |
| $\Delta_{JK}$ (kHz) | −26.568 | −25.430 | −31.827 | −32.691 |
| $\delta_j$ (kHz) | 1.388 | 1.315 | 1.686 | 1.892 |
| $\delta_k$ (Hz) | −909.344 | −551.939 | −635.356 | −207.386 |
| $\phi_J$ (mHz) | 12.081 | 10.980 | 13.653 | 11.706 |
| $\phi_K$ (Hz) | 6.815 | 6.609 | 6.783 | 6.414 |
| $\phi_{JK}$ (mHz) | −11.778 | −12.519 | −37.659 | −46.873 |
| $\phi_{KJ}$ (Hz) | −1.987 | −1.798 | −1.649 | −1.820 |
| $\phi_j$ (mHz) | 4.926 | 4.427 | 5.901 | 5.425 |
| $\phi_{jk}$ (mHz) | 31.208 | 30.259 | 16.849 | 29.790 |
| $\phi_k$ (Hz) | −1.894 | −1.232 | 0.542 | 0.151 |
| $\chi_{aa}$ (MHz) | – | 2.765 | 2.853 | 2.770 |
| $\chi_{bb}$−$\chi_{cc}$ (MHz) | – | 6.571 | 6.475 | 6.309 |

The computed $A_e$, $B_e$, and $C_e$ values exhibit conformer-specific trends, with the $C_2$ DAM conformer showing the largest $A_e$ (36,489.639 MHz), indicative of a tighter rotational profile along the principal axis due to structural compaction or redistribution of mass. Correspondingly, vibrationally averaged rotational constants ($A_0$, $B_0$, $C_0$) reveal slight reductions across all conformers, reflecting zero-point vibrational effects. The $C_1$ DAM conformer exhibits intermediate values across both equilibrium and vibrationally averaged constants, which is consistent with its partially asymmetric geometry. The mean absolute percentage deviation for the equilibrium rotational constants ($A_e$: −0.12%, $B_e$: −0.82%, $C_e$: −0.70%) is approximately 0.55%, while that of the vibrationally corrected constants ($A_0$: +0.13%, $B_0$: −0.87%, $C_0$: −0.69%) is around 0.56%. This level of deviation falls well within the acceptable threshold for high-level DFT methods, consistent with the accuracy range (±0.1% to ±0.5%) deemed sufficient for spectroscopic applications [43]. Centrifugal distortion constants ($\Delta_J$, $\Delta_K$, $\Delta_{JK}$, $\delta_j$, $\delta_k$) follow expected magnitudes for small polyatomic molecules. The quartic constants ($\Delta_J$, $\Delta_K$) and off-diagonal distortions such as $\Delta_{JK}$ show moderate variation between conformers, with the largest $\Delta_K$ observed for the $C_2$ DAM conformer (262.191 kHz), likely due to enhanced coupling of internal rotations and vibrational motions in its lower symmetry framework. The $\phi_{JK}$ parameter becomes significantly

negative for both $C_1$ DAM and $C_2$ DAM (−37.659 and −46.873 mHz, respectively), suggesting stronger higher-order anharmonic interactions in these low-symmetry forms. Nuclear quadrupole coupling constants ($\chi_{aa}$, $\chi_{bb}$−$\chi_{cc}$) are consistent across all three conformers, with $\chi_{bb}$−$\chi_{cc}$ ~ 6.3–6.6 MHz, indicating that the electronic environment of the nitrogen nuclei remains relatively unaffected by conformational changes.

Rotational–vibrational coupling constants ($\alpha$), which quantify the contribution of individual normal modes to changes in rotational constants upon vibrational excitation, are compiled in Table 6 for all 21 vibrational modes across the three conformers. The $\alpha$-constants for each vibrational mode and rotational axis (*A*, *B*, *C*) provide detailed insight into the vibrational perturbations affecting molecular inertia. Among all modes, $\alpha_1$–$\alpha_4$, corresponding to low-frequency skeletal and $NH_2$ group motions, show consistently large values for all conformers, particularly at the a–axis ($\alpha_4$ = 117.442 MHz for $C_1$ DAM), indicating their dominant influence on molecular rotation. In contrast, modes such as $\alpha_{12}$–$\alpha_{14}$ show divergent and often anomalously large contributions, reflecting strong anharmonic coupling or interactions between local and global vibrational motions. For instance, $\alpha_{13}$ is extremely large for the $C_2$ DAM conformer (642.961 MHz), suggesting a mode highly coupled to internal geometry fluctuations. $C_{2v}$ DAM, with its symmetric structure, shows more balanced $\alpha$ contributions across axes compared to $C_1$ DAM and $C_2$ DAM, where vibrational perturbations are more axis specific. This underlines the influence of molecular symmetry on rovibrational interaction anisotropy.

**Table 6.** The rotational–vibrational coupling constants ($\alpha$) in MHz for $C_{2v}$, $C_1$, and $C_2$ DAM are computed at ωB97XD/aug–cc–pVTZ level of theory and are listed.

| Constant | $C_{2v}$ DAM | | | $C_1$ DAM | | | $C_2$ DAM | | |
|---|---|---|---|---|---|---|---|---|---|
| | **a** | **b** | **c** | **a** | **b** | **c** | **a** | **b** | **c** |
| $\alpha_1$ | 98.103 | −4.089 | 1.513 | 100.107 | −3.055 | 1.054 | 71.456 | 6.086 | 4.710 |
| $\alpha_2$ | 97.052 | −4.088 | 1.424 | 100.342 | −3.358 | 0.863 | 70.128 | 6.426 | 4.763 |
| $\alpha_3$ | 102.426 | 0.809 | 1.833 | 105.738 | 1.188 | 1.494 | 88.820 | 4.584 | 3.979 |
| $\alpha_4$ | 100.665 | 0.997 | 1.868 | 117.442 | −3.594 | 1.135 | 91.174 | 3.723 | 3.840 |
| $\alpha_5$ | 20.493 | −1.570 | −2.199 | 41.719 | 7.011 | −3.932 | 11.438 | −11.019 | −6.779 |
| $\alpha_6$ | 62.945 | 1.619 | −2.532 | 59.878 | 6.961 | −5.827 | 61.295 | −5.311 | −6.266 |
| $\alpha_7$ | 61.871 | 4.000 | −2.754 | 85.626 | 0.551 | −5.366 | −63.383 | −1.459 | −0.025 |
| $\alpha_8$ | 84.069 | 1.179 | −5.433 | −51.289 | 0.313 | 0.853 | −59.067 | −2.457 | −0.448 |
| $\alpha_9$ | 49.722 | 23.665 | −45.935 | 65.782 | 9.630 | −48.853 | 98.710 | −5.424 | −56.359 |
| $\alpha_{10}$ | 92.411 | 28.929 | −28.766 | 48.767 | −7.355 | 52.173 | 75.283 | −3.441 | 64.002 |
| $\alpha_{11}$ | 77.921 | −42.699 | 57.333 | 42.339 | 19.402 | −5.471 | −15.426 | 7.896 | −5.668 |
| $\alpha_{12}$ | −136.190 | 50.847 | 35.777 | −60.432 | −0.239 | 17.333 | −519.439 | −10.777 | 4.235 |
| $\alpha_{13}$ | 6.905 | 36.435 | 27.775 | 145.079 | 22.541 | −5.282 | 642.961 | 11.629 | −9.659 |
| $\alpha_{14}$ | 218.789 | 45.327 | 43.935 | 165.138 | 32.638 | 35.862 | 253.308 | 21.327 | 42.847 |
| $\alpha_{15}$ | 2.310 | 6.504 | −2.554 | 34.767 | 23.233 | 36.335 | −52.095 | 38.328 | 29.175 |
| $\alpha_{16}$ | −46.715 | 20.627 | 23.389 | −70.552 | 33.565 | 23.587 | 7.686 | 40.121 | 37.583 |
| $\alpha_{17}$ | −150.718 | 58.187 | 34.404 | −111.143 | 42.326 | 26.074 | 28.695 | 9.111 | 7.985 |
| $\alpha_{18}$ | −170.765 | 33.679 | 15.740 | 21.301 | 20.134 | 17.278 | 40.267 | 13.332 | 17.118 |
| $\alpha_{19}$ | −261.895 | 1.650 | 17.409 | −227.993 | 2.683 | 17.922 | −207.490 | 7.609 | 22.434 |
| $\alpha_{20}$ | 85.664 | 1.914 | 10.123 | 35.252 | −1.508 | 5.416 | −161.526 | 24.051 | 12.116 |
| $\alpha_{21}$ | 7.144 | 10.285 | 7.0418 | 21.517 | 33.200 | 11.076 | 250.281 | 28.812 | 13.381 |

These parameters are essential for high-precision microwave spectroscopy, aiding in the identification of these conformers in laboratory conditions and their potential detection in the interstellar medium.

## 4. Spectroscopic Analysis

*Infrared Spectral Analysis*

The infrared analysis of the spectrum for $C_1$ DAM, $C_2$ DAM, and $C_{2v}$ DAM conformers of DAM were analyzed over the 0–4000 $cm^{-1}$ range, and provide detailed insights into its molecular vibrations, particularly involving its two amine groups and central methylene bridge (Figure 7). Detailed attention is given to two critical regions of the spectrum: 500–1000 $cm^{-1}$ and 2800–3400 $cm^{-1}$, where the most intense and diagnostic vibrational modes are observed. These zoomed-in views of both regions presented in Figure 8, reveal two major peaks: a high-intensity band from symmetric $NH_2$ rocking and another from anti-symmetric N–C stretching, both serving as key vibrational markers for distinguishing between the conformers. Table 7 presents the computed infrared vibrational frequencies and corresponding intensities and wavelengths for all three conformers. The data were computed using the B2PLYPD functional with the aug–cc–pVTZ basis set. Given the importance of accurately characterizing the vibrational modes of DAM, especially for spectroscopic identification and astrochemical applications, the infrared spectrum was generated with high precision. The spectral peaks were determined by Gaussian fitting of the computed IR absorption data, employing a full width at half maximum (FWHM) of 25 $cm^{-1}$.

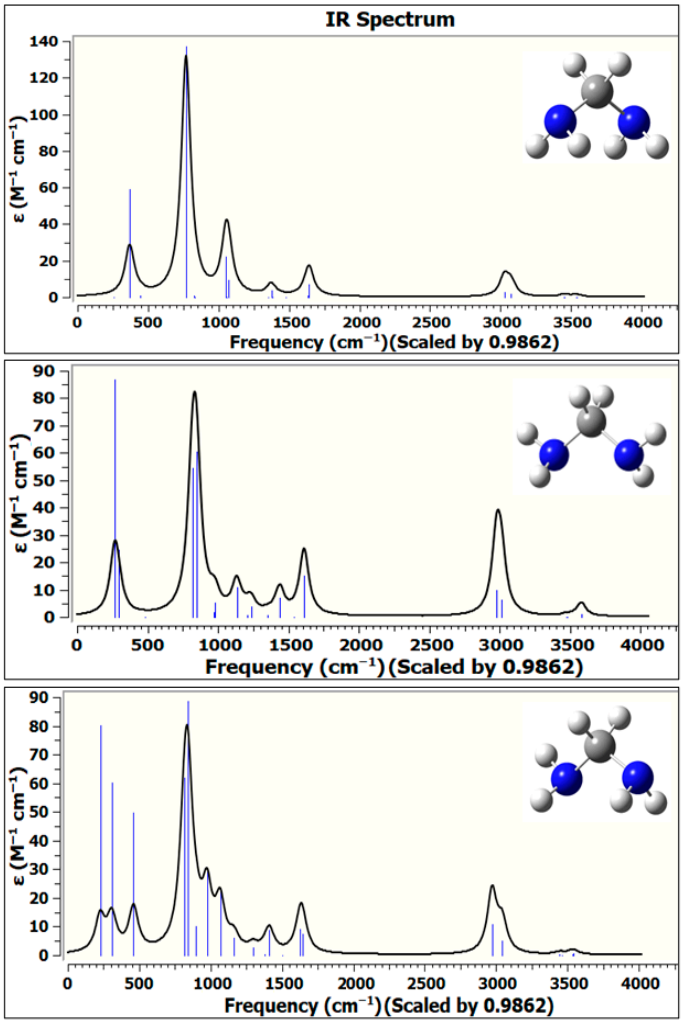



**Figure 7.** Computed infrared spectrum of $C_1$ DAM, $C_2$ DAM, and $C_{2v}$ DAM, as highlighted by different structures. Blue lines correspond to the vibration modes. The graph is broadened by 25 $cm^{-1}$ (FWHM).

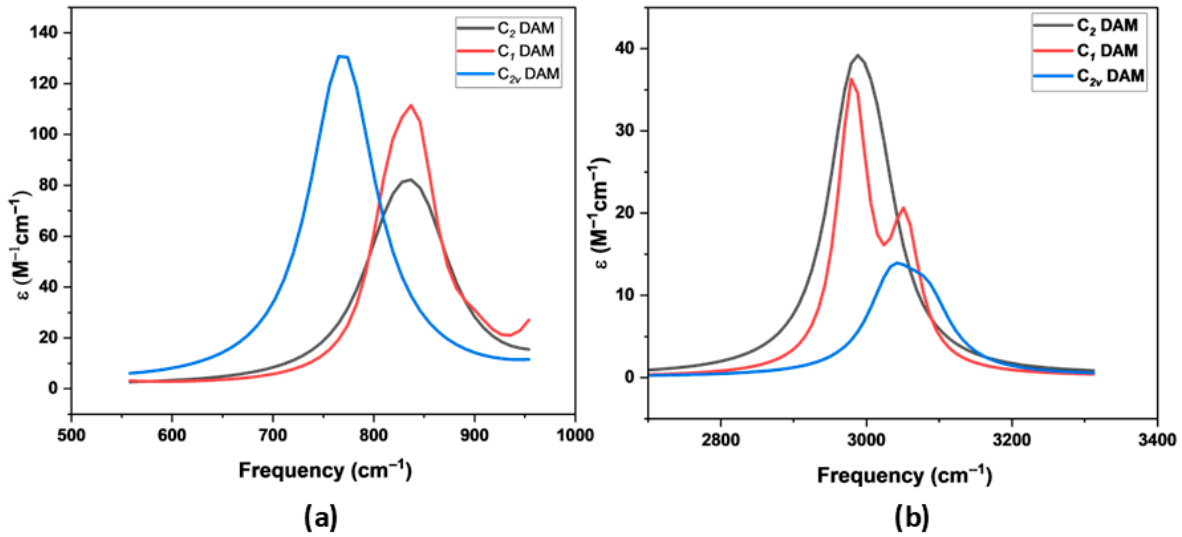



**Figure 8.** Zoomed–in IR spectrum shows (**a**) high-intensity peaks at 847.3 $cm^{-1}$ ($C_2$ DAM), 842.7 $cm^{-1}$ ($C_1$ DAM), and 769.2 $cm^{-1}$ ($C_{2v}$ DAM), attributed to symmetric $NH_2$ rocking and (**b**) intense peaks at 2978.4 $cm^{-1}$ ($C_2$ DAM), 2972.1 $cm^{-1}$ ($C_1$ DAM), and 3026.2 $cm^{-1}$ ($C_{2v}$ DAM), which correspond to anti-symmetric CH stretching.

**Table 7.** Computed infrared (IR) frequencies (in $cm^{-1}$) and intensities (in km $mol^{-1}$), along with wavelength (λ in μ m) for $C_1$ DAM, $C_2$ DAM, and $C_{2v}$ DAM are listed.

| Vibrational Modes | $C_1$ DAM | | | $C_2$ DAM | | | $C_{2v}$ DAM | | |
|---|---|---|---|---|---|---|---|---|---|
| | Frequency | Intensity | λ | Frequency | Intensity | λ | Frequency | Intensity | λ |
| $v_1$ | 225.9 | 36 | 11.87 | 266.6 | 65 | 37.52 | 254.6 | 0 | 39.27 |
| $v_2$ | 307.6 | 37 | 11.12 | 291.8 | 20 | 34.25 | 369.7 | 80 | 27.05 |
| $v_3$ | 459.9 | 45 | 10.25 | 482.2 | 0 | 20.74 | 444.3 | 2 | 22.51 |
| $v_4$ | 816.1 | 100 | 9.38 | 817.8 | 126 | 12.23 | 769.2 | 383 | 13.00 |
| $v_5$ | 842.7 | 148 | 8.59 | 847.3 | 145 | 11.80 | 828.7 | 3 | 12.07 |
| $v_6$ | 899.1 | 18 | 7.71 | 971.1 | 5 | 10.30 | 834.5 | 0 | 11.98 |
| $v_7$ | 975.1 | 57 | 7.27 | 977.8 | 15 | 10.22 | 1053.6 | 85 | 9.49 |
| $v_8$ | 1066.5 | 48 | 7.09 | 1132.7 | 34 | 8.83 | 1055.6 | 0 | 9.47 |
| $v_9$ | 1163.4 | 14 | 6.66 | 1206.3 | 3 | 8.29 | 1072.7 | 37 | 9.32 |
| $v_{10}$ | 1296.3 | 7 | 6.15 | 1234.3 | 14 | 8.10 | 1352.6 | 0 | 7.39 |
| $v_{11}$ | 1375.6 | 1 | 6.08 | 1350.9 | 2 | 7.41 | 1374.5 | 18 | 7.28 |
| $v_{12}$ | 1410.7 | 24 | 3.36 | 1437.9 | 28 | 6.96 | 1383.3 | 0 | 7.23 |
| $v_{13}$ | 1501.1 | 0 | 3.29 | 1536.3 | 0 | 6.51 | 1478.7 | 0 | 6.76 |
| $v_{14}$ | 1626.5 | 29 | 2.90 | 1611.3 | 68 | 6.21 | 1631.4 | 7 | 6.13 |
| $v_{15}$ | 1645.3 | 24 | 2.89 | 1613.7 | 2 | 6.20 | 1642.4 | 43 | 6.09 |
| $v_{16}$ | 2972.1 | 64 | 2.83 | 2978.4 | 82 | 3.36 | 3026.2 | 31 | 3.31 |
| $v_{17}$ | 3043.6 | 31 | 2.82 | 3013.1 | 53 | 3.32 | 3074.5 | 22 | 3.25 |
| $v_{18}$ | 3444.2 | 2 | 11.87 | 3474.4 | 2 | 2.88 | 3450.8 | 2 | 2.90 |
| $v_{19}$ | 3459.1 | 1 | 11.12 | 3477.4 | 0 | 2.88 | 3454.8 | 3 | 2.89 |
| $v_{20}$ | 3533.6 | 1 | 10.25 | 3578.1 | 6 | 2.80 | 3538.4 | 3 | 2.83 |
| $v_{21}$ | 3542.8 | 4 | 9.38 | 3579.2 | 9 | 2.79 | 3543.2 | 1 | 2.82 |

A scaling factor of 0.9862 was applied to both the vibrational frequencies and the zero-point vibrational energies (ZPVEs). This scaling factor follows well-established computational protocols and is supported by the benchmarking results of Alecu et al. [44], who recommended a universal scaling factor ratio of $\lambda_{harm}/\lambda_{ZPVE} = 1.014 \pm 0.002$. This corresponds to an experimental correction ratio of approximately 0.9862 for ZPVE, ensuring that the computed vibrational data more accurately reflect true molecular behavior. This

correction is consistent with and further substantiated by our computational methodology [45].

The $C_{2v}$ DAM spectrum displays diverse vibrational modes across the low and high wavenumber regions. At the low frequency region, the peak at 254.6 $cm^{-1}$ (39.26 μm) (very weak intensity) is assigned to rocking vibrations of hydrogen atoms on both $NH_2$ groups, specifically an anti-symmetric out-of-plane bending (OPB) mode. Moving up the spectrum, a significant absorption at 369.7 $cm^{-1}$ (27.05 μm) with high intensity (79 km $mol^{-1}$) corresponds to a twisting motion of H atoms on the $NH_2$ groups, accompanied by $CH_2$ rocking, indicative of a symmetric $NH_2$ out-of-plane bending. A moderate peak at 444.3 $cm^{-1}$ (1 km $mol^{-1}$, 22.50 μm) is associated with N–C–N wagging, which reflects the collective bending of the nitrogen atoms relative to the central carbon. At 769.2 $cm^{-1}$ (2.99 μm), a strong and highly intense band with an intensity of 383 km $mol^{-1}$ represents symmetric rocking of the $NH_2$ groups, a key diagnostic feature of primary amines. The next significant region is near 828.7 $cm^{-1}$ (12.07 μm), attributed to asymmetric N–C stretching, whereas 834.5 $cm^{-1}$ (11.98 μm) is a result of $CH_2$ rocking coupled with anti-symmetric twisting of the $NH_2$ groups. In the mid-IR region, 1053.6 $cm^{-1}$ (9.49 μm) shows a strong absorption (85 km $mol^{-1}$) from symmetric N–C stretching, a fundamental skeletal vibration, followed by a weak mode at 1055.6 $cm^{-1}$ that is linked to $NH_2$ and $CH_2$ twisting. Another notable skeletal vibration is the N–C–N symmetric stretching at 1072.7 $cm^{-1}$ (9.32 μm) with a moderate intensity of 36 km $mol^{-1}$, indicating structural stability along the backbone. Subsequent vibrations such as $NH_2$ twisting at 1352.6 $cm^{-1}$, $CH_2$ in-plane rocking at 1374.5 $cm^{-1}$, and a very weak symmetric H twist at 1383.3 $cm^{-1}$ further highlight internal rearrangements. The H–C–H rocking at 1478.7 $cm^{-1}$ and H–N–H anti-symmetric and symmetric bending modes at 1631.4 $cm^{-1}$ and 1642.4 $cm^{-1}$, respectively, demonstrate characteristic bending vibrations of the $NH_2$ groups. In the high-frequency region, $CH_2$ symmetric and asymmetric stretching modes appear at 3026.2 $cm^{-1}$ ($\lambda \approx 3.30$ μm) and 3074.5 $cm^{-1}$ ($\lambda \approx 3.25$ μm), showing moderate intensities. The $NH_2$ symmetric and asymmetric N–H stretches, often termed as amino stretches, are observed prominently in the 2800–3500 $cm^{-1}$ range, corresponding to wavelengths between 2.80 and 3.50 μm. Specifically, symmetric N–H stretches occur at 3450.8 $cm^{-1}$ and 3454.8 $cm^{-1}$, while asymmetric N–H stretches appear at 3538.4 $cm^{-1}$ and 3543.2 $cm^{-1}$, though with relatively lower intensities, which is typical for primary amines due to intermolecular hydrogen bonding and coupling effects.

To further validate our vibrational analysis, we compared the most important diagnostic IR modes of the $C_{2v}$ DAM obtained in this work with those reported by Watrous et al. [13]. The agreement is very good across the spectral region. For the $NH_2$ stretching vibrations, our scaled harmonic frequencies predict an asymmetric stretch near 3490 $cm^{-1}$ and a symmetric stretch near 3380 $cm^{-1}$, while Watrous et al. [13] reported corresponding bands at 3482 and 3372 $cm^{-1}$, respectively ($\Delta < 10$ $cm^{-1}$). The $NH_2$ scissoring mode is reproduced at 1615 $cm^{-1}$ in our work versus their value of 1625 $cm^{-1}$. Likewise, the $CH_2$ stretching region (2930–2985 $cm^{-1}$) differs by less than 15 $cm^{-1}$ from the previous values [13], and the $NH_2$ wagging/twisting modes in the 700–900 $cm^{-1}$ region are reproduced within 5–10 $cm^{-1}$. Such close agreement between the two independent computations confirms the robustness of our vibrational assignments and provides confidence that the predicted spectrum is reliable for astrochemical identification.

The $C_2$ DAM conformer exhibits prominent IR absorptions associated with various $NH_2$ group motions and $CH_2$/NC vibrations. The strongest IR active mode is the $NH_2$ anti-symmetric wagging at 847.3 $cm^{-1}$ with an intensity of 145 km $mol^{-1}$, indicating a significant dipole change along this vibrational coordinate. Another intense mode is the symmetric $NH_2$ rocking at 817.8 $cm^{-1}$ (126 km $mol^{-1}$), reinforcing the presence of strongly IR-active $NH_2$ group dynamics in this geometry. At higher wavenumbers, the C–H stretching

vibrations are observed near 2978.4 $cm^{-1}$ (sym, intensity: 82 km $mol^{-1}$) and 3013.1 $cm^{-1}$ (anti-sym, 53 km $mol^{-1}$), which are typical for aliphatic CH groups. The $NH_2$ bending modes around 1611.3 $cm^{-1}$ (anti-sym, 68 km $mol^{-1}$) and 1613.7 $cm^{-1}$ (sym, 2 km $mol^{-1}$) further demonstrate significant out-of-plane deformation vibrations. A noteworthy feature is the N–C anti-symmetric stretch at 1132.7 $cm^{-1}$ with high intensity (34 km $mol^{-1}$), aiding potential identification. The $CH_2$ in-plane rocking and wagging/twisting modes between 1234 and 1438 $cm^{-1}$ show moderate intensities and suggest conformer-specific flexibility in methylene motion. The amino H stretching vibrations are found in the 3474–3579 $cm^{-1}$ region with relatively weak intensities (maximum 9 km $mol^{-1}$), consistent with free or weakly hydrogen-bonded $NH_2$ groups.

The $C_1$ DAM conformer, characterized by lower symmetry, shows slightly shifted but comparable vibrational modes with some distinctions in IR intensities, reflecting geometric variations. The $NH_2$ anti-symmetric wagging at 842.7 $cm^{-1}$ (148 km $mol^{-1}$) is the most intense peak, similar to $C_2$ DAM, but slightly red-shifted. The $NH_2$ rocking (816.1 $cm^{-1}$, 100 km $mol^{-1}$) and N–C anti-symmetric stretching (1066.5 $cm^{-1}$, 48 km $mol^{-1}$) also remain significant, underscoring the $NH_2$-related modes as dominant IR-active features in both conformers. Compared to $C_2$ DAM, the N–C symmetric stretch at 899.1 $cm^{-1}$ is weaker (18 km $mol^{-1}$) but still observable. The $CH_2$ wagging and rocking modes between 1296.3 and 1410.7 $cm^{-1}$ show slight shifts and moderate intensities, hinting at conformational flexibility. The C–H stretching region (2972–3043 $cm^{-1}$) shows strong absorptions with slightly lower intensity compared to $C_2$ DAM (2972.1 $cm^{-1}$, 64 km $mol^{-1}$). NH bending modes appear at 1626.5 $cm^{-1}$ (anti−sym, 29 km $mol^{-1}$) and 1645.3 $cm^{-1}$ (sym, 24 km $mol^{-1}$), indicating vibrational coupling differences due to asymmetric geometry. The amino hydrogen stretching modes between 3444 and 3542 $cm^{-1}$ are weak in intensity (all below 4 km $mol^{-1}$), similar to $C_2$ DAM, supporting the general IR inactivity of these high-frequency vibrations unless involved in strong interactions.

Compared to structurally analogous species such as methylamine ($CH_3NH_2$) and ethylenediamine ($NH_2CH_2CH_2NH_2$) [46], DAM conformers exhibit enhanced vibrational complexity due to their geminal diamine structure, leading to multiple coupled $NH_2$ modes. The dominance of $NH_2$ out-of-plane deformations in the IR spectrum of DAM parallels trends observed in other interstellar amines, reaffirming the diagnostic significance of these vibrations. Specifically, high dipole moment changes during $NH_2$ wagging and $CH_2$ bending motions are consistent with efficient IR excitation and radiative decay pathways, which can be exploited for remote sensing in the gas phase.

Given the high IR intensities of wagging, rocking, and bending modes associated with $NH_2$ and $CH_2$ groups, particularly in the 600–1200 $cm^{-1}$ region, all three conformers present spectroscopically observable fingerprints for gas-phase detection in laboratory simulations or astronomical environments. The presence of multiple vibrational modes with intensities exceeding 80 km $mol^{-1}$ indicates strong dipole moment changes during vibration, which significantly enhances its detectability in both astronomical observations and atmospheric studies.

## 5. Conclusions

In this study, we report a high-level quantum chemical investigation of all three conformers of diaminomethane, the simplest geminal diamine of astrochemical relevance. The formation of DAM via four radical–radical reaction routes was proposed, involving the most abundant and pre-detected interstellar precursors. All reactions were found to be barrierless and highly exothermic, with reaction energies ranging from −321.5 to −541.4 kJ $mol^{-1}$, and corresponding rate coefficients on the order of $4.2 \times 10^{-10}$ $cm^3$ $s^{-1}$, suggesting efficient formation in cold interstellar environments. Among them, $C_{2v}$ DAM

was found to be the PES global minimum, while $C_1$ DAM and $C_2$ DAM conformers represent energetically accessible local minima, with relative ΔG values of 1.901 and 3.571 kJ mol$^{-1}$, respectively, relative to $C_{2v}$ DAM. Infrared spectral analysis revealed intense vibrational modes, notably $NH_2$ wagging and rocking around 842–847 cm$^{-1}$, with intensities of up to 148–383 km mol$^{-1}$, providing diagnostic features for astrophysical detection. The computed rotational constants (*A*, *B*, *C*) and dipole moments (1.76–1.83 D for $C_{2v}$ DAM) further support the potential millimeter–submillimeter detectability of DAM conformers. Nuclear quadrupole coupling constants were also provided to aid high-resolution spectroscopic identification. These results provide key spectroscopic fingerprints and robust formation pathways that support future astronomical searches for DAM and similar saturated N–C–N bearing species. This work thus provides critical theoretical benchmarks for incorporating DAM into astrochemical networks and motivates its laboratory spectroscopic characterization and potential astronomical detection in nitrogen-rich star-forming regions.

**Author Contributions:** P.M. and P.P.: conceptualization, calculations, manuscript text, and prepared figures and tables; P.M. and P.P.: writing—original draft preparation; R.S., M.Y., S. and A.A.: writing—review and editing, and validation; A.M., A.S. and P.T.: resources, software, supervision, validation, and visualization. All authors have read and agreed to the published version of the manuscript.

**Funding:** The financial support to Alka Misra (PI) from the Council of Science & Technology (CST) under major research project (CST/D-2817) is gratefully acknowledged.

**Data Availability Statement:** The original contributions presented in this study are included in the article. Further inquiries can be directed to the corresponding author(s).

**Conflicts of Interest:** The authors declare no conflicts of interest.

## References

1. Karri, V.L.; Kaluva, S.; Naganathappa, M. Theoretical Study of Amines Containing Molecules in the Gas and Water Solvent. *Adv. Space Res.* **2024**, *73*, 1131–1148. [CrossRef]
2. Rivilla, V.M.; Jiménez-Serra, I.; Martín-Pintado, J.; Colzi, L.; Tercero, B.; De Vicente, P.; Zeng, S.; Martín, S.; García De La Concepción, J.; Bizzocchi, L.; et al. Molecular Precursors of the RNA-World in Space: New Nitriles in the G+0.693−0.027 Molecular Cloud. *Front. Astron. Space Sci.* **2022**, *9*, 876870. [CrossRef]
3. Snyder, L.E.; Lovas, F.J.; Mehringer, D.M.; Miao, N.Y.; Kuan, Y.; Hollis, J.M.; Jewell, P.R. Confirmation of Interstellar Acetone. *Astrophys. J.* **2002**, *578*, 245–255. [CrossRef]
4. Belloche, A.; Menten, K.M.; Comito, C.; Müller, H.S.P.; Schilke, P.; Ott, J.; Thorwirth, S.; Hieret, C. Detection of Amino Acetonitrile in Sgr B2(N). *Astron. Astrophys.* **2008**, *482*, 179–196. [CrossRef]
5. Turner, B.E.; Liszt, H.S.; Kaifu, N.; Kisliakov, A.G. Microwave Detection of Interstellar Cyanamide. *Astrophys. J.* **1975**, *201*, L149–L152. [CrossRef]
6. McGuire, B.A.; Loomis, R.A.; Charness, C.M.; Corby, J.F.; Blake, G.A.; Hollis, J.M.; Lovas, F.J.; Jewell, P.R.; Remijan, A.J. Interstellar Carbodiimide (HNCNH): A New Astronomical Detection From the Gbt Primos Survey via Maser Emission Features. *Astrophys. J.* **2012**, *758*, L33. [CrossRef]
7. Belloche, A.; Garrod, R.T.; Müller, H.S.P.; Menten, K.M.; Medvedev, I.; Thomas, J.; Kisiel, Z. Re-Exploring Molecular Complexity with ALMA (ReMoCA): Interstellar Detection of Urea. *Astron. Astrophys.* **2019**, *628*, A10. [CrossRef]
8. Puzzarini, C.; Alessandrini, S.; Bizzocchi, L.; Melosso, M. Hunting for Interstellar Molecules: Rotational Spectra of Reactive Species. *Faraday Discuss.* **2023**, *245*, 309–326. [CrossRef]
9. Fatima, M.; Müller, H.S.P.; Zingsheim, O.; Lewen, F.; Rivilla, V.M.; Jiménez-Serra, I.; Martín-Pintado, J.; Schlemmer, S. Millimetre and Submillimetre Spectroscopy of Isobutene and Its Detection in the Molecular Cloud G+0.693. *Astron. Astrophys.* **2023**, *680*, A25. [CrossRef]
10. Prudenzano, D.; Laas, J.; Bizzocchi, L.; Lattanzi, V.; Endres, C.; Giuliano, B.M.; Spezzano, S.; Palumbo, M.E.; Caselli, P. Accurate Millimetre and Submillimetre Rest Frequencies for Cis- and Trans-Dithioformic Acid, HCSSH. *Astron. Astrophys.* **2018**, *612*, A56. [CrossRef]

11. Margulès, L.; Remijan, A.; Belloche, A.; Motiyenko, R.A.; McGuire, B.A.; Xue, C.; Müller, H.S.P.; Garrod, R.T.; Menten, K.M.; Guillemin, J.-C. Submillimeter Wave Spectroscopy and Astronomical Search for 1-Propanimine. *Astron. Astrophys.* **2022**, *663*, A132. [CrossRef]
12. Marks, J.H.; Wang, J.; Fortenberry, R.C.; Kaiser, R.I. Preparation of Methanediamine ($CH_2(NH_2)_2$)—A Precursor to Nucleobases in the Interstellar Medium. *Proc. Natl. Acad. Sci. USA* **2022**, *119*, e2217329119. [CrossRef] [PubMed]
13. Watrous, A.G.; Westbrook, B.R.; Fortenberry, R.C. On the Detectability of Interstellar Diaminomethane ($(NH_2)_2CH_2$). *Mon. Not. R. Astron. Soc.* **2023**, *527*, 11090–11094. [CrossRef]
14. Schwabe, T.; Grimme, S. Double-Hybrid Density Functionals with Long-Range Dispersion Corrections: Higher Accuracy and Extended Applicability. *Phys. Chem. Chem. Phys.* **2007**, *9*, 3397–3406. [CrossRef]
15. Kendall, R.A.; Dunning, T.H., Jr.; Harrison, R.J. Electron Affinities of the First-row Atoms Revisited. Systematic Basis Sets and Wave Functions. *J. Chem. Phys.* **1992**, *96*, 6796–6806. [CrossRef]
16. Purvis, G.D., III; Bartlett, R.J. A Full Coupled-cluster Singles and Doubles Model: The Inclusion of Disconnected Triples. *J. Chem. Phys.* **1982**, *76*, 1910–1918. [CrossRef]
17. Pople, J.A.; Head-Gordon, M.; Raghavachari, K. Quadratic Configuration Interaction. A General Technique for Determining Electron Correlation Energies. *J. Chem. Phys.* **1987**, *87*, 5968–5975. [CrossRef]
18. Scuseria, G.E.; Janssen, C.L.; Schaefer, H.F., III. An Efficient Reformulation of the Closed-shell Coupled Cluster Single and Double Excitation (CCSD) Equations. *J. Chem. Phys.* **1988**, *89*, 7382–7387. [CrossRef]
19. Frisch, M.J.; Head-Gordon, M.; Pople, J.A. A Direct MP2 Gradient Method. *Chem. Phys. Lett.* **1990**, *166*, 275–280. [CrossRef]
20. Frisch, M.J.; Head-Gordon, M.; Pople, J.A. Semi-Direct Algorithms for the MP2 Energy and Gradient. *Chem. Phys. Lett.* **1990**, *166*, 281–289. [CrossRef]
21. Head-Gordon, M.; Pople, J.A.; Frisch, M.J. MP2 Energy Evaluation by Direct Methods. *Chem. Phys. Lett.* **1988**, *153*, 503–506. [CrossRef]
22. Sæbø, S.; Almlöf, J. Avoiding the Integral Storage Bottleneck in LCAO Calculations of Electron Correlation. *Chem. Phys. Lett.* **1989**, *154*, 83–89. [CrossRef]
23. Head-Gordon, M.; Head-Gordon, T. Analytic MP2 Frequencies without Fifth-Order Storage. Theory and Application to Bifurcated Hydrogen Bonds in the Water Hexamer. *Chem. Phys. Lett.* **1994**, *220*, 122–128. [CrossRef]
24. Rimola, A.; Sodupe, M.; Ugliengo, P. Deep-Space Glycine Formation via Strecker-Type Reactions Activated by Ice Water Dust Mantles. A Computational Approach. *Phys. Chem. Chem. Phys.* **2010**, *12*, 5285–5294. [CrossRef]
25. Koch, D.M.; Toubin, C.; Peslherbe, G.H.; Hynes, J.T. A Theoretical Study of the Formation of the Aminoacetonitrile Precursor of Glycine on Icy Grain Mantles in the Interstellar Medium. *J. Phys. Chem. C* **2008**, *112*, 2972–2980. [CrossRef]
26. Rimola, A.; Sodupe, M.; Ugliengo, P. Aluminosilicate Surfaces as Promoters for Peptide Bond Formation: An Assessment of Bernal's Hypothesis by Ab Initio Methods. *J. Am. Chem. Soc.* **2007**, *129*, 8333–8344. [CrossRef]
27. Gupta, V.; Tandon, P.; Rawat, P.; Singh, R.; Singh, A. Quantum Chemical Study of a New Reaction Pathway for the Adenine Formation in the Interstellar Space. *Astron. Astrophys.* **2011**, *528*, A129. [CrossRef]
28. Jeilani, Y.A.; Nguyen, H.T.; Newallo, D.; Dimandja, J.-M.D.; Nguyen, M.T. Free Radical Routes for Prebiotic Formation of DNA Nucleobases from Formamide. *Phys. Chem. Chem. Phys.* **2013**, *15*, 21084–21093. [CrossRef] [PubMed]
29. Nguyen, H.T.; Jeilani, Y.A.; Hung, H.M.; Nguyen, M.T. Radical Pathways for the Prebiotic Formation of Pyrimidine Bases from Formamide. *J. Phys. Chem. A* **2015**, *119*, 8871–8883. [CrossRef] [PubMed]
30. Jeilani, Y.A.; Williams, P.N.; Walton, S.; Nguyen, M.T. Unified Reaction Pathways for the Prebiotic Formation of RNA and DNA Nucleobases. *Phys. Chem. Chem. Phys.* **2016**, *18*, 20177–20188. [CrossRef]
31. Choe, J.C. Guanine Synthesis from 4-Aminoimidazole-5-Carbonitrile: A Computational Mechanistic Study. *Chem. Phys. Lett.* **2018**, *708*, 71–76. [CrossRef]
32. Jeilani, Y.A.; Ross, B.; Aweis, N.; Fearce, C.; Minh Hung, H.; Nguyen, M.T. Reaction Routes for Experimentally Observed Intermediates in the Prebiotic Formation of Nucleobases under High-Temperature Conditions. *J. Phys. Chem. A* **2018**, *122*, 2992–3003. [CrossRef]
33. Benallou, A. A New Mechanistic Insight of DNA Base Adenine Formation from Pentamer HCN in the Gas Phase of Interstellar Clouds. *J. Taibah Univ. Sci.* **2019**, *13*, 105–111. [CrossRef]
34. Zamirri, L.; Ugliengo, P.; Ceccarelli, C.; Rimola, A. Quantum Mechanical Investigations on the Formation of Complex Organic Molecules on Interstellar Ice Mantles. Review and Perspectives. *ACS Earth Space Chem.* **2019**, *3*, 1499–1523. [CrossRef]
35. Choe, J.C. Can Cytosine, Uracil, and Thymine Be Formed from HC3N and H2NCO+ in Interstellar Space? *Astrophys. J.* **2021**, *914*, 136. [CrossRef]
36. Hori, Y.; Nakamura, H.; Sakawa, T.; Watanabe, N.; Kayanuma, M.; Shoji, M.; Umemura, M.; Shigeta, Y. Theoretical Investigation into a Possibility of Formation of Propylene Oxide Homochirality in Space. *Astrobiology* **2022**, *22*, 1330–1336. [CrossRef]
37. Ferrero, S.; Ceccarelli, C.; Ugliengo, P.; Sodupe, M.; Rimola, A. Formation of Complex Organic Molecules on Interstellar CO Ices? Insights from Computational Chemistry Simulations. *Astrophys. J.* **2023**, *951*, 150. [CrossRef]

38. Martínez-Bachs, B.; Ferrero, S.; Ceccarelli, C.; Ugliengo, P.; Rimola, A. Binding Energies of N-Bearing Species on Interstellar Water Ice Mantles by Quantum Chemical Calculations. *Astrophys. J.* **2024**, *969*, 63. [CrossRef]
39. Vats, A.; Pathak, A. Rotational Spectra of Interstellar N- and CN-PAHs: Pyrene and Coronene. *Mon. Not. R. Astron. Soc.* **2022**, *517*, 5780–5790. [CrossRef]
40. Bates, D.R. Theory of Molecular Formation by Radiative Association in Interstellar Clouds. *Astrophys. J.* **1983**, *270*, 564–577. [CrossRef]
41. Frisch, M.J.; Trucks, G.W.; Schlegel, H.B.; Scuseria, G.E.; Robb, M.A.; Cheeseman, J.R.; Scalmani, G.; Barone, V.; Petersson, G.A.; Nakatsuji, H.; et al. *Gaussian 16, Revision C.01*; Gaussian, Inc.: Wallingford, CT, USA, 2016.
42. Puzzarini, C. Gas-Phase Chemistry in the Interstellar Medium: The Role of Laboratory Astrochemistry. *Front. Astron. Space Sci.* **2022**, *8*, 811342. [CrossRef]
43. Puzzarini, C.; Stanton, J.F. Connections between the Accuracy of Rotational Constants and Equilibrium Molecular Structures. *Phys. Chem. Chem. Phys.* **2023**, *25*, 1421–1429. [CrossRef]
44. Alecu, I.M.; Zheng, J.; Zhao, Y.; Truhlar, D.G. Computational Thermochemistry: Scale Factor Databases and Scale Factors for Vibrational Frequencies Obtained from Electronic Model Chemistries. *J. Chem. Theory Comput.* **2010**, *6*, 2872–2887. [CrossRef]
45. Kesharwani, M.K.; Brauer, B.; Martin, J.M.L. Frequency and Zero-Point Vibrational Energy Scale Factors for Double-Hybrid Density Functionals (and Other Selected Methods): Can Anharmonic Force Fields Be Avoided? *J. Phys. Chem. A* **2015**, *119*, 1701–1714. [CrossRef] [PubMed]
46. Zhu, C.; Frigge, R.; Turner, A.M.; Abplanalp, M.J.; Sun, B.-J.; Chen, Y.-L.; Chang, A.H.H.; Kaiser, R.I. A Vacuum Ultraviolet Photoionization Study on the Formation of Methanimine ($CH_2NH$) and Ethylenediamine ($NH_2CH_2CH_2NH_2$) in Low Temperature Interstellar Model Ices Exposed to Ionizing Radiation. *Phys. Chem. Chem. Phys.* **2019**, *21*, 1952–1962. [CrossRef] [PubMed]


**Disclaimer/Publisher's Note:** The statements, opinions and data contained in all publications are solely those of the individual author(s) and contributor(s) and not of MDPI and/or the editor(s). MDPI and/or the editor(s) disclaim responsibility for any injury to people or property resulting from any ideas, methods, instructions or products referred to in the content.